Marine and Petroleum Geology 64 (2015) 152–164

Contents lists available at ScienceDirect

Marine and Petroleum Geology

journal homepage: www.elsevier.com/locate/marpetgeo

Research paper

Mechanical and petrophysical behavior of organic-rich chalk from the Judea Plains, Israel

Ksenia Bisnovat [a], Yossef H. Hatzor [a, *], Harold J. Vinegar [a, b], Scott V. Nguyen [b], Vyacheslav Palchik [a], Shimon Feinstein [a]

[a] Department of Geological Environmental Sciences, Ben-Gurion University of the Negev, Beer-Sheva 84105, Israel
[b] Israel Energy Initiatives Ltd., Jerusalem 45408, Israel

ARTICLE INFO

Article history:
Received 18 August 2014
Received in revised form
20 November 2014
Accepted 22 February 2015
Available online 5 March 2015

Keywords:
Mechanical behavior
Porosity
Permeability
Organic rich chalk
Source rock
Oil shale

ABSTRACT

The geomechanical and petrophysical properties of the Late Cretaceous organic-rich chalk from the Shefela basin in central Israel were studied using laboratory tests performed on solid cylindrical samples from core retrieved from the resource. The investigated section includes two formations, the Ghareb and the Mishash of central Israel. The Shefela chalk is dark brown and rich in organic matter, with up to 20% TOC at the middle of the Ghareb formation. Both uniaxial compressive strength and Young's modulus of the chalk display stress dependency with the mean values increasing with depth. The tensile strength parallel to the bedding is found to be higher by 1.7 on average for Ghareb and by 2.2 on average for Mishash compared to the tensile strength normal to the bedding. Unconfined compressive strength appears to increase with total organic carbon (TOC) whereas the effect of TOC on tensile strength and elasticity is less conclusive. A linear compression–dilation boundary is defined for the Shefela chalk based on analysis of uniaxial and triaxial test results. The porosity is high, approx. 37% at the Ghareb formation, decreasing to 32% at the Mishash formation. The permeability is very low, ranging between 0.001 mD and 1 mD, and exhibits strong anisotropy with a vertical to horizontal ratio of 0.2. The porosity and permeability are found to be independent of the variation in organic content, confirming co-precipitation of the calcite minerals and organic matter during deposition.

1. Introduction

Source rocks are fine-grained sedimentary rocks containing organic matter called 'kerogen' that yields oil and gas upon thermal maturation (Hutton, 1987; Tissot and Welte, 1984). Source rocks were deposited in a variety of depositional environments where the combination of primary production and preservation conditions were favorable for organic matter accumulation in the sediments, from Precambrian to Tertiary worldwide. Upon exposure to sufficient heating conditions, generally temperature and time, either under natural burial or in unaerobic reactors, the organic matter decomposes and acts as source rocks for petroleum and natural gas (Dyni, 2003). The hydrocarbon yield of the source rock is a function of the organic matter content and chemical composition, which is determined primarily by the type of organic matter assemblages and depositional and diagenetic environments.

Once considered as only source rocks in conventional petroleum systems, these matured organic-rich rocks now act as self-sourcing reservoirs in unconventional oil and gas developments. The advent of multi-stage hydraulic fracturing in long horizontal wells has made possible the economic development of these low permeability systems. Within the United States, oil production from these types of reservoirs now accounts for 45% of total production or over 3.5 million bbl per day (Ratner and Tiemann, 2014). Self-sourcing reservoirs are found worldwide, and the exploration and development of these resources are in the early phases.

Immature source rocks, also known as oil shale, which have not yet generated oil and gas can also be significant energy resources. Oil shale is usually found at shallow depths and retains its full potential for hydrocarbon generation upon thermal maturation. Using in situ thermal recovery methods, oil and gas can be generated from oil shale by heating the rock to induce thermal maturation of the organic matter (Ryan et al., 2010). Oil shale deposits in

* Corresponding author. Tel.: +972 8 6472621; fax: +972 8 6428717.
E-mail address: hatzor@bgu.ac.il (Y.H. Hatzor).

http://dx.doi.org/10.1016/j.marpetgeo.2015.02.044
0264-8172/

the world range in size from small occurrences to enormous masses that occupy thousands of square kilometers and in age from Precambrian to Tertiary. According to the 2010 World Energy Outlook by the International Energy Agency, the world oil shale resources may be the equivalent of more than 5 trillion barrels (790×10^9 m^3) of oil in place of which more than 1 trillion barrels (160×10^9 m^3) may be technically produced (IEA, 2010).

In the source rocks and oil shale, the organic matters are the remains of algae and plankton, and other cellular remains of lacustrine and marine environments. The organic matter is mixed with various amounts of fine-grained mineral matter. The composition of the inorganic fraction may vary from shale where clay minerals are predominant, such as the Lower Jurassic shales of Western Europe (particularly France and West Germany), to carbonates with subordinate amounts of clay and other minerals, such as the Green River shales of Colorado, Utah and Wyoming (Tissot and Vandenbroucke, 1983). The organic fraction consists of 5–15% of the rock though it may reach as high as 60%. The mechanical and petrophysical properties of the source rocks and oil shale are therefore significantly affected by the organic phase, the mineralogical composition and dynamic processes. The study of their mechanical and petrophysical behavior is essential for the evaluation of the these formations as a potential resource of energy that can be produced by either hydraulic fracturing in the case of self-sourcing reservoirs or in situ thermal recovery in the case of oil shale reservoirs.

In this paper we study the mechanical and petrophysical behavior of two immature organic – rich chalk formations from the Judea Plains in Israel, locally known as the Late Cretaceous Ghareb and Mishash formations of the Mount Scopus group.

2. Geological setting of study area

Some thirty sub-basins containing Late Cretaceous organic-rich carbonates were described in Israel (Minster, 2009), which are part of a very long belt developed in an upwelling system along the Late Cretaceous southern margin of the Tethys ocean (Almogi-Labin et al., 1993). The kerogen of the Israeli oil shale is mainly type IIs (Spiro, 1980). The deposits extend over approximately 15% of Israel's area where the total resources are estimated to be larger than 300 billion tons of rock (Minster, 2009). In several localities in central and southern Israel, the organic matter-rich sequences reach a thickness of 200–400 m, and in certain thick sections represent a major portion of the Mount Scopus Group. The organic – rich deposits that are associated with the Mount Scopus Group are typically found in synclinal structures. These structures contributed to the preservation of the organic matter, as well as the global anoxic event of the Upper Cretaceous. Carbonates like chalk, marl and limestone comprise the mineral constituents, while the organic component is dispersed in the matrix or micro-laminated.

The Shefela basin, found in the Shefela and the East coastal plain areas of central Israel, is the largest of the oil shale bearing basins in Israel and among the largest in the Levant (Fig. 1). It extends across more than 1000 km^2 and contains the thickest oil shale succession, estimated at 100–500 m (Burg et al., 2010; Gvirtzman et al., 1985; Minster, 2009). The resource was estimated at 300-350 billion tons of mainly organic rich carbonate rocks (Minster, 2009). The section enriched with organic matter is part of the Mount Scopus group. The thickness of Mount Scopus group varies due to the folding and subsidence of the synclinal basins during its sedimentation, resulting in asymmetric synclinal structure at the Shefela basin. The organic rich succession in the Shefela basin accumulated on the continental slope, marginally to the main upwelling center for a duration of about 10 m y between

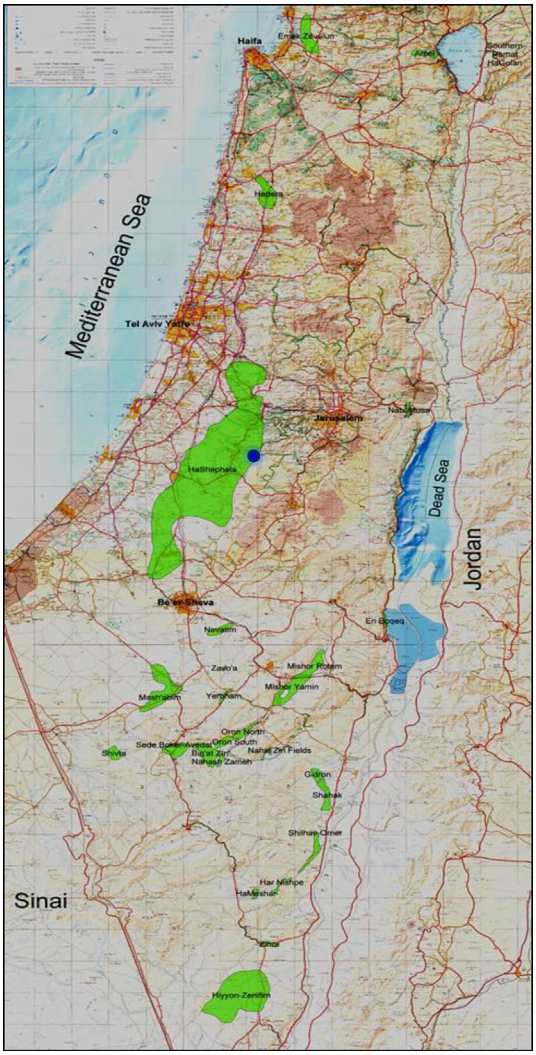

Figure 1. Oil shale deposits in Israel (Minster, 2009). The blue circle represents the location of the Aderet borehole. (For interpretation of the references to color in this figure legend, the reader is referred to the web version of this article.)

middle Campanian and late Maastrichtian, is the longest known organic-rich deposition in all of the Levant (Almogi-Labin et al., 1993; Eshet et al., 1994).

In this paper we focus on the Late Cretaceous (Campanian – Maastrichtian) oil shale succession as explored in the Aderet borehole ranging from a depth of 265–600 m (Fig. 2). The Aderet well is located in the northwest of the Shfela basin (see Fig. 1) and was one of six appraisal wells drilled by Israel Energy Initiatves, Ltd. Core from the full interval was made available for this study. The oil shale unit shows vertical lithological uniformity in the Ghareb formation and in transition to the upper Mishash formation. It consists of mostly dark brown chalk, rich in organic matter and large visible fossils, accompanied by thin marl beds in places, some phosphate and small pyrite crystals. There are hardly any open fissures and no visible bedding. The “Mishash tongue” appears as a thin layer of chert, organic rich chalk and phosphate. Below it, the chalk becomes brighter with depth, indicating the decrease in organic matter; silicification can be noticed (Burg et al., 2010).

As can be seen in Figure 2, the total organic carbon (TOC) content as measured from samples taken from the core average 15% in the middle of the Aderet section (350–450 m) and decrease to about 10% TOC above and below.

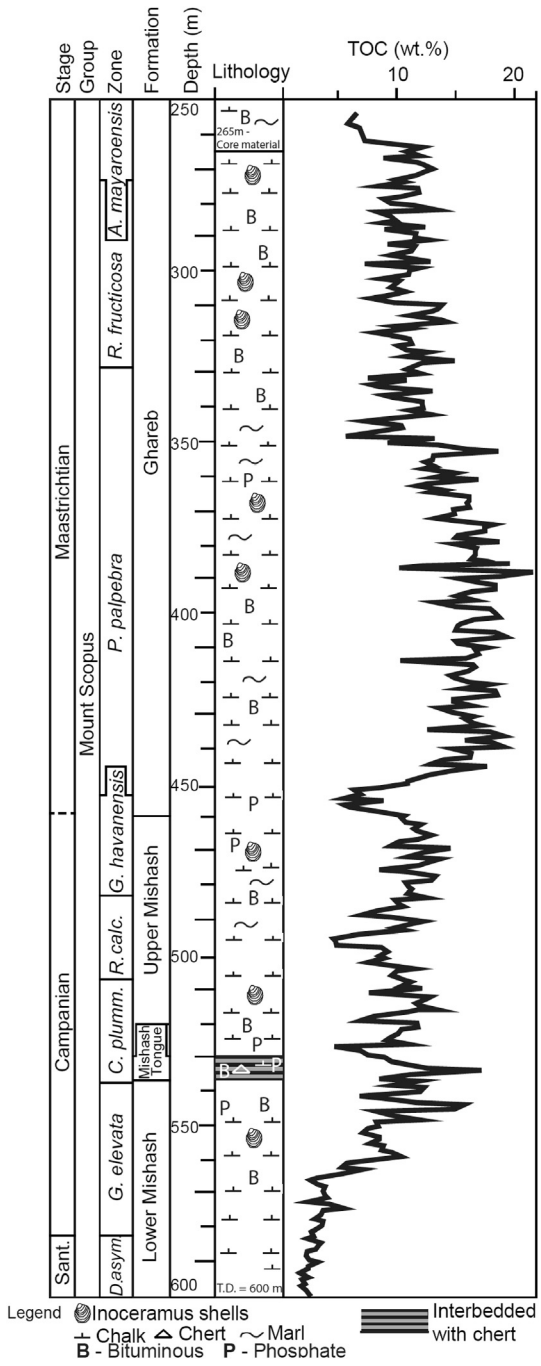

Figure 2. Aderet well: Late Cretaceous (Santonian–Maasrichtian) stratigraphy and lithological section and total organic carbon (TOC). Modified from (Meilijson et al., 2014).

3. Experimental methods

3.1. Testing program and sample preparation

A comprehensive core analysis program was conducted on core samples extracted from the Aderet well in order to best characterize the mechanical and petrophysical behavior of the Late Cretaceous organic-rich chalk The nominal length of the cores that were extracted from the field was 100 cm and the nominal diameter was 8.4 cm. The cores were wrapped in the field and sealed in a plastic tube before they were brought to the lab. The following tests were performed:

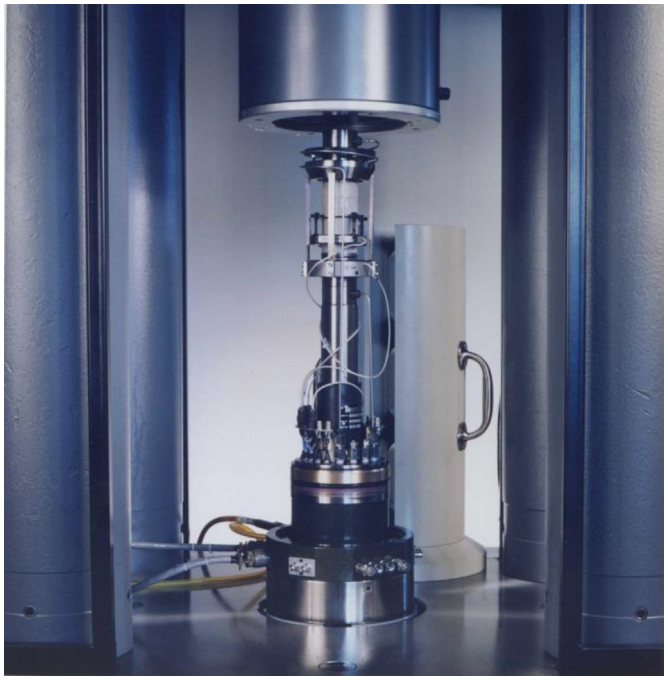

Figure 3. A detail of the stiff, hydraulic, closed-loop, servo-controlled load frame (TerraTek systems model FX-S-33090) used to perform hydrostatic, uniaxial, and triaxial compression tests showing the sample stack and the position of the axial and radial strain cantilever gages. The core diameter shown is 54 mm.

- Unconfined, triaxial and hydrostatic compression tests were performed using a hydraulic, stiff, closed-loop servo controlled system (Fig. 3). Results include static elastic constants, compressional strength under unconfined and confined conditions, dilational behavior, and a representative failure criterion

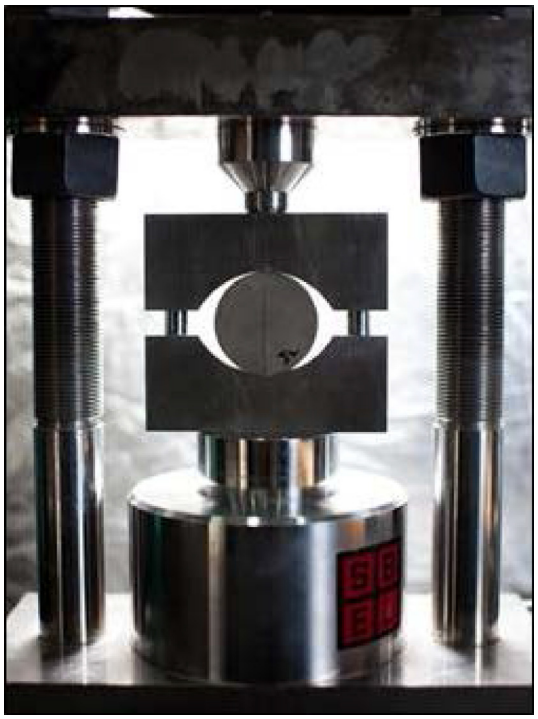

Figure 4. The manual mini–load frame (SBEL model PLT-75) used for Brazilian tests. A 54 mm diameter oil shale sample is shown after testing. Note the vertical tensile fracture which developed along the centerline of the tested disc.

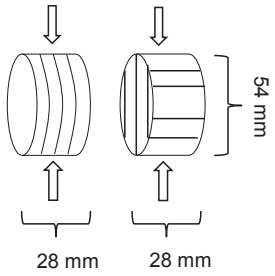

Figure 5. Relationship between loading direction and bedding direction in the indirect Brazilian tension tests. The configuration in the left panel provides the tensile strength parallel to bedding whereas in the right panel the tensile strength normal to bedding is obtained.

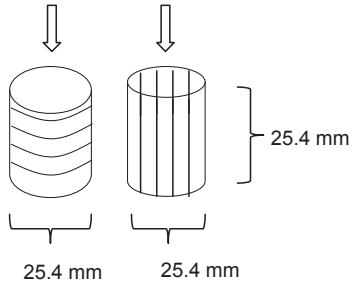

Figure 6. The relationship between flow direction and bedding direction in permeability tests. The configuration in the left panel provides the permeability normal to bedding whereas in the right panel the permeability parallel to bedding is obtained.

for compression. These tests were performed on 54 mm diameter (2 1/8″ – NX size) right solid cylinders with length to diameter ratio of about 2.0. All cores in this group of tests were prepared with their long axis normal to bedding, as in the original cores that were brought from the field; therefore the effect of mechanical anisotropy could not be explored in these tests. The measurement output from the two radial strain transducers mounted on the sample parallel to the bedding direction however (see Fig. 3) allowed confirmation of transverse isotropy assumption within the bedding plane direction. While mechanical anisotropy was not studied in these tests, the loading direction with respect to the bedding plane direction was similar to field conditions and therefore the results

Table 1
Concentrated results for Uniaxial compression tests.

Sample	Depth, m	ρ_t, gr/cm^3	ω, %	TOC, %	E, GPa	ν	σ_c, MPa
AD1-11a	291	1.44	5.41	12.54	1.11	0.20	16.15
AD1-27c	341	1.80	23.93	7.62	2.75	0.32	12.71
AD1-34b	358	1.60	13.92	10.37	1.76	0.27	16.24
AD1-40b	376	1.34	1.65	16.78	1.98	0.21	27.47
AD1-55a	420	1.67	25.49	17.14	1.90	0.26	19.65
AD1-64c	449	1.74	23.00	12.35	2.82	0.26	20.78
AD1-104b	572	1.87	0.64	3.30	9.18	0.21	52.83
AD1-113b	599	2.02	1.15	1.94	8.05	0.18	54.68

ρ_t is bulk density, ω is water content at which the test was performed, TOC is total organic carbon in wt%, E and ν are Young's modulus and Poisson's ratio and σ_c is Uniaxial compressive strength.

Table 2
Concentrated results for triaxial compression tests.

Sample	Depth, m	ρ_t, gr/cm^3	ω, %	TOC, %	E, GPa	ν	$\Delta\sigma$ (MPa)	σ_3, at peak (MPa)	σ_1, at peak (MPa)
AD1-27c2	341	1.81	26.45	9.90	1.44	0.16	13.20	1.22	14.42
AD1-28a	342	1.71	21.40	9.10	4.11	0.40	16.65	2.61	19.26
AD1-26a	336	1.88	24.32	9.11	1.69	0.16	14.77	3.2	17.97
AD1-26a2	336	1.85	24.13	8.50	1.63	0.40	13.70	4.55	18.25
AD1-29b	346	1.79	26.17	10.93	1.49	0.29	15.7	3.78	19.48

ρ_t is bulk density, ω is water content at which the test was performed, TOC is total organic carbon in wt%, E and ν are Young's modulus and Poisson's ratio, $\Delta\sigma$ is the peak stress difference, σ_3 is the confining pressure at peak and σ_1 is the axial stress at peak.

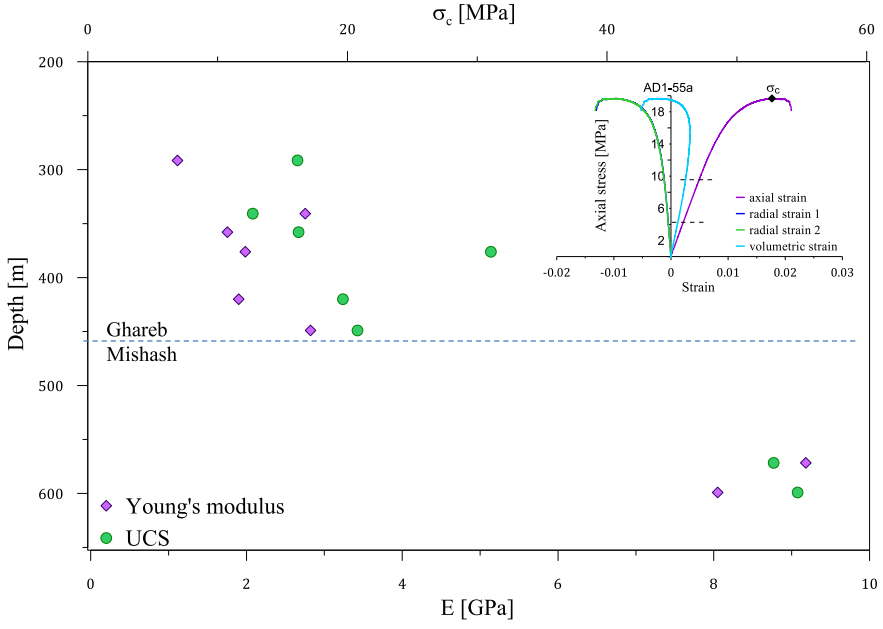

Figure 7. Main: Enhancement of uniaxial compressive strength and Young's modulus with depth; the green circles and the purple diamonds represent the uniaxial compressive strength and Young's modulus, respectively; the dashed blue line represents the boundary between the Ghareb and the Mishash Formations. Inset: Stress strain curve for uniaxial compression test of sample AD1-55a, legend: – axial strain, – radial strain1, – radial strain2, – volumetric strain, the dashed lines represent the linear elastic segment and the black diamond represents the point of peak uniaxial strength. (For interpretation of the references to color in this figure legend, the reader is referred to the web version of this article.)

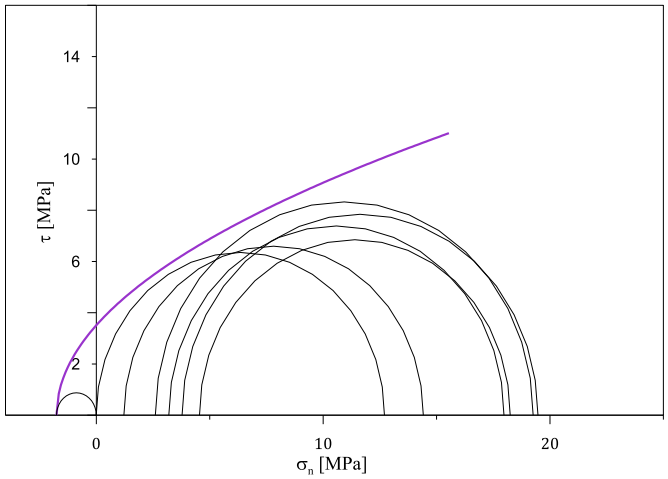

Figure 8. Mohr circles for principal stresses at failure obtained from uniaxial tension (Brazilian), uniaxial compression, and triaxial tests. The modified Griffith's failure criterion for compression in shear vs. normal stress space is delineated in purple. (For interpretation of the references to color in this figure legend, the reader is referred to the web version of this article.)

obtained are assumed to be applicable for the field applications. Indirect (Brazilian) tensile strength tests were performed using a manual, hydraulic, mini-load frame (Fig. 4). 54 mm diameter right solid cylinders with L/D ratio of 0.5 were used for these tests. Samples were prepared in two orthogonal directions so that in one case (left panel in Fig. 5) the tensile stress developed within the plane of isotropy thus providing the tensile strength parallel to bedding, and in the other (right panel of Fig. 5) the tensile stress developed in direction normal to bedding thus providing the tensile strength normal to bedding. Recall that in the Brazilian testing methodology the tensile stress develops in the horizontal direction across from the vertical centerline of the cylinder where ultimately the tensile fracture develops at failure (see Fig. 4). . A subset of the samples for the Brazilian tests was partially oven dried to study the dependence on moisture content.

- Porosity, permeability and Klinkenberg slip factor tests were performed using an unsteady state gas permeameter & porosimeter device. 25.4 mm (1″) diameter right solid cylinders with L/D ratio of 1.0 were used for these tests. Samples were prepared in two orthogonal directions providing the normal to bedding (left panel of Fig. 6) and parallel to bedding (right panel of Fig. 6) permeability. These samples were oven dried at a temperature of 110 °C for 24 h.

Table 3
Results for hydrostatic tests.

Sample	Depth, m	K, MPa	ω, %	TOC, %
AD1-4c	274	1293	2.93	8.66

Sample	Depth, m	K_1, MPa	K_2, MPa	K_3, MPa	ω, %	TOC, %
AD1-27b	341	1471	3287	4850	24.69	7.28

K is the static bulk modulus, ω is water content at which the test was performed and TOC is total organic carbon in wt%.

The ends of all solid cylinder samples for the mechanical and petrophysical tests described above were polished to a roughness smaller than 0.01 mm.

Samples that were destructively tested were ground and measured for total organic carbon (TOC) using carbon analyzer model SC632 from LECO Corp. For samples that were not destructively tested, TOC was measured on twin samples from the same core.

3.2. Compression experiments

Compression experiments were performed using a hydraulic triaxial testing system manufactured by TerraTek systems, model FX-S-33090. The stiff load frame was operated using a closed-loop, servo control with maximum axial force of 1.4 MN, stiffness of 5×10^9 N/m, and confining pressure capacity of 70 MPa. Piston displacement, axial load, axial (ε_a), and radial strains (ε_{r1}, ε_{r2}) were continuously monitored for feedback during the closed-loop servo-controlled tests (Fig. 3). Unconfined and triaxial compression tests were run at a constant strain rate of 1×10^{-5} s^{-1}. Testing was continued beyond peak stress and terminated when the axial strain reached 2% axial strain.

Eight samples from various depths of the Aderet section were tested under unconfined compression, and five samples from a depth interval of 335–346 m were tested under triaxial

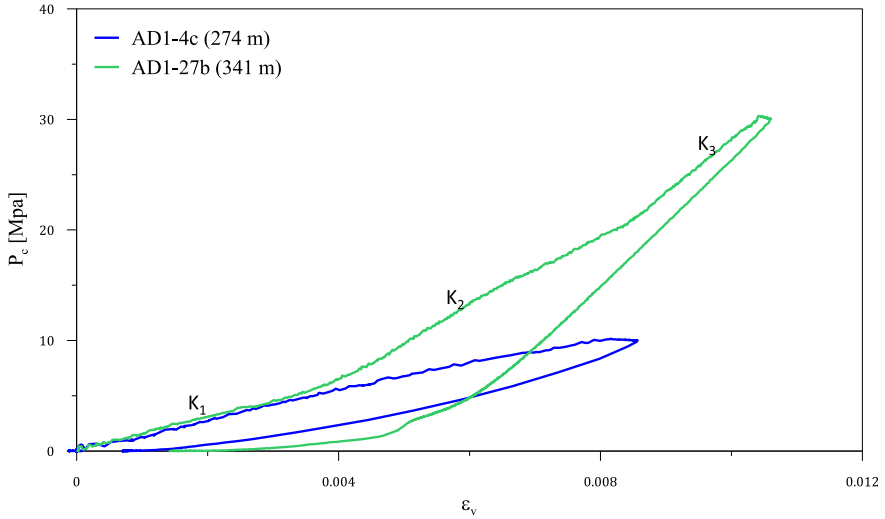

Figure 9. The entire load and unload history for the hydrostatic compression tests of samples AD1-4c (blue plot) and AD1-27b (green plot). (For interpretation of the references to color in this figure legend, the reader is referred to the web version of this article.)

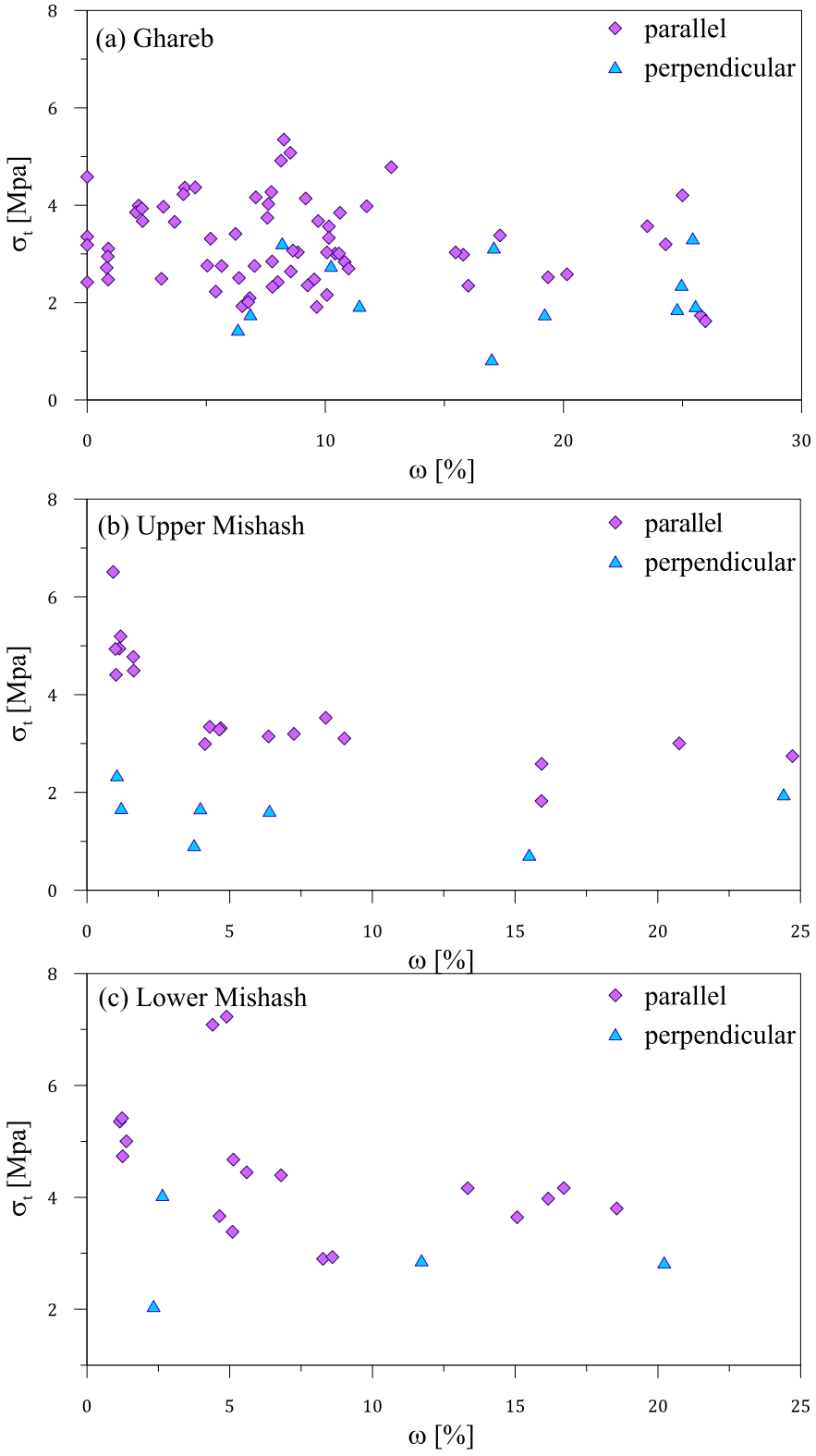

Figure 10. Tensile strength as a function of water content both parallel (purple diamonds) and perpendicular (blue triangles) to bedding direction: (a) Ghareb Formation; (b) Upper Mishash Formation; (c) Lower Mishash Formation. (For interpretation of the references to color in this figure legend, the reader is referred to the web version of this article.)

compression. The water content of the samples during testing varied as the samples were air dried after sample preparation procedures such as drilling, sawing, and end grinding were performed with water as the cooling agent. The triaxial tests were performed under initial confining pressures of 1 MPa, 2 MPa, 3 MPa, 4 MPa, 5 MPa and 10 MPa. As the confining pressure pump was controlled manually, we were not able to react precisely to volume changes and maintain a constant value of confining pressure

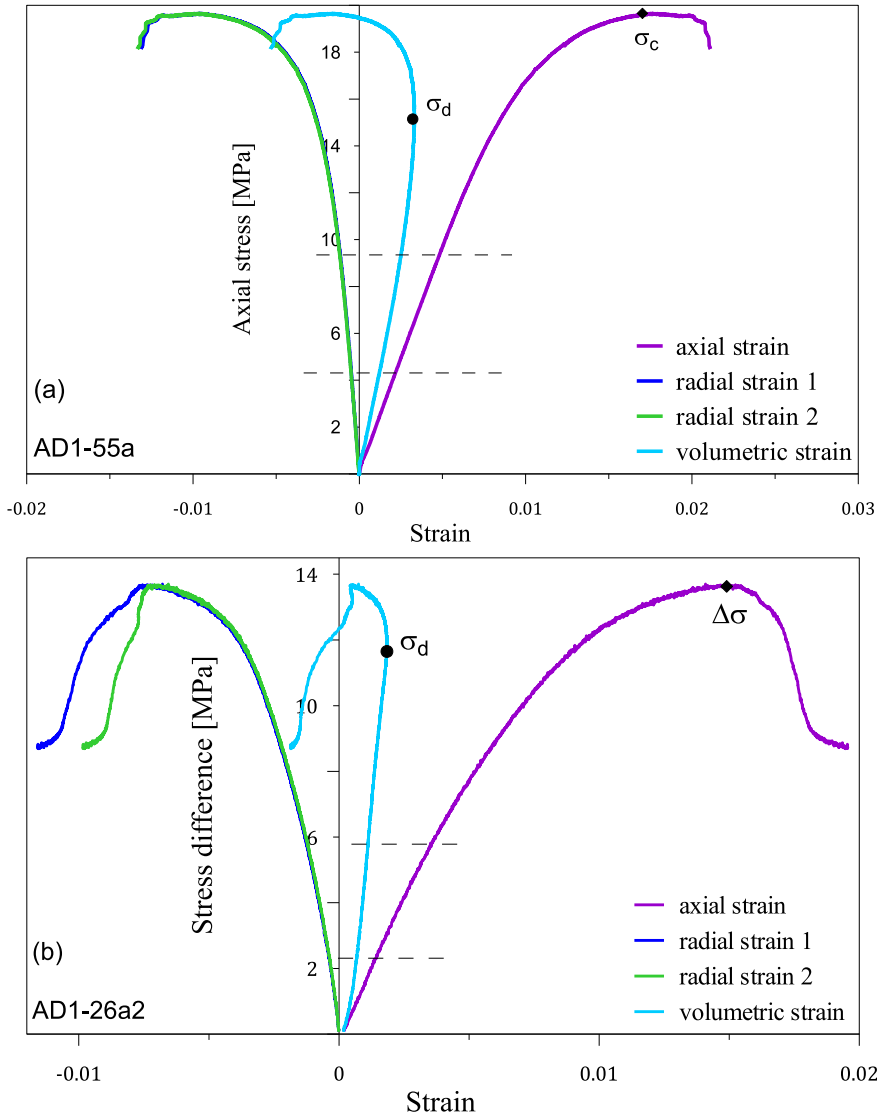

Figure 11. Stress strain curve for: (a) uniaxial compression test of sample AD1-55a, (b) triaxial compression test of sample AD1-26a2; legend: - axial strain, - radial strain1, - radial strain2, - volumetric strain, the dashed lines represent the linear elastic segment, the black circle represent the onset of dilation point and the black diamond represents the point of peak uniaxial strength σ_c at (a) and the point of peak stress difference $\Delta\sigma$ at (b).

throughout the test. Two samples were tested under hydrostatic conditions up to maximum confining pressures of 10 MPa and 30 MPa.

3.3. Tensile (Brazilian) tests

A total of 128 indirect tensile (Brazilian) strength tests were performed using a manual, hydraulic, mini-load frame manufactured by ELE systems Inc. (SBEL model PLT-75). Loading was applied by two diametrically opposed concave loading jaws until failure of the sample was achieved (Fig. 4). The influence of water content on the tensile strength was examined by testing samples at various water content conditions. Mechanical anisotropy was tested by measuring the tensile strength differences between samples drilled parallel and perpendicular to the bedding direction (Fig. 5).

3.4. Porosity and permeability measurements

Porosity (ϕ), Klinkenberg-corrected gas permeability (k_∞), and Klinkenberg slip factor (b) were determined on 236 samples with an unsteady state gas permeameter & porosimeter Coreval 30 device manufactured by Vinci Technologies. Nitrogen gas was used for the porosity measurements and nitrogen for the permeability measurements. The porosity and permeability tests were run in sequence with a single loading of the sample at a confining pressure of 400 psi. Anisotropy was examined by measuring the permeability in samples drilled both parallel and perpendicular to the bedding direction (Fig. 6).

4. Rock mechanics test results

4.1. Compressive strength and deformability

The compressive strength of the rock was determined from the point at which maximum stress was achieved; Young's modulus (E) and Poisson's ratio (ν) were calculated using linear regressions along the linear segment of the axial stress–strain curve (see Fig. 7). The obtained results for the 8 tested samples are summarized in Table 1. Both uniaxial compressive strength and Young's modulus display stress dependency with values clearly increasing with

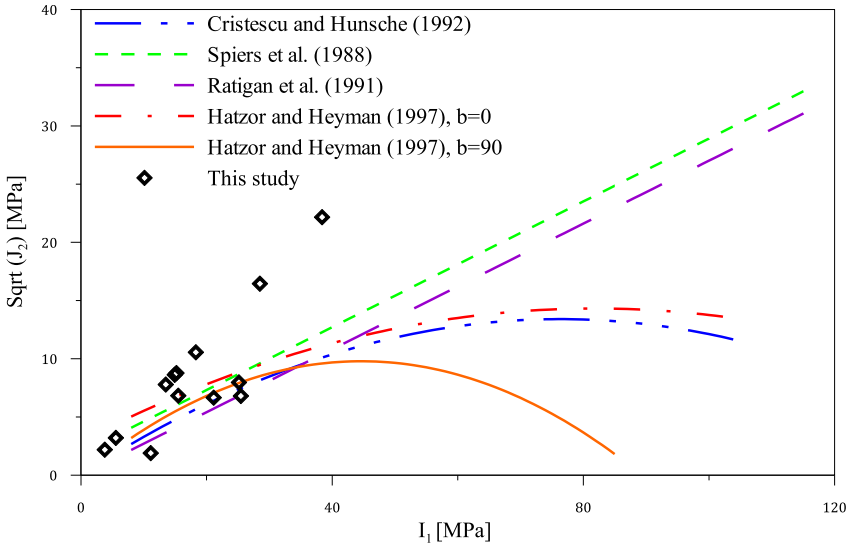

Figure 12. Different models for compression–dilation boundary (after Van Sambeek et al. (1993) and Hatzor and Heyman (1997)) and results of this study. Legend: Cristescu and Hunsche (1992), Spiers et al. (1988), Ratigan et al. (1991), Hatzor and Heyman (1997) $\beta = 0$, Hatzor and Heyman (1997) $\beta = 90$, black diamonds represent this study.

Table 4
Summary of coefficients values for the different CD boundaries in terms of stress invariants, the coefficients fit an equation from the form $J_2 = aI_1^2 + bI_1 + c$; β represents the angle between the axis of maximum stress and the anisotropy (bedding) direction ($\beta = 0°$ is compression normal to bedding direction and $\beta = 90°$ is compression parallel to bedding direction).

Model	*a*	*b*	*c* (MPa)
Cristescu and Hunsche (1992)	−0.0023	0.3511	0
Spiers et al. (1988)	0	0.27	1.9
Ratigan et al. (1991)	0	0.27	0
Hatzor and Heyman (1997); $\beta = 0°$	−0.0017	0.28	2.9
Hatzor and Heyman (1997); $\beta = 90°$	−0.0048	0.44	0

Table 5
Fitting coefficients values for the C–D boundary of the Shefela oil shale in terms of stress invariants, the coefficients fit an equation from the form of $J_2 = aI_1^2 + bI_1 + c$.

Model	*a*	*b*	*c* (MPa)
Shefela oil shale	0	0.5026	−0.69

depth (Fig. 7). The static Young's modulus for the Ghareb formation increases from ~1 GPa at 290 m depth up to ~3 GPa at the bottom of the Ghareb Formation at 460 m depth. The underlying Mishash Formation which is characterized by more silicified chalk, have higher values reaching up to 9.2 GPa at 600 m. The average uniaxial compressive strength for the Ghareb and Mishash formations is 19 MPa and 53.8 MPa, respectively.

The shear strength of the Ghareb formation was tested at a depth interval of 335 m–345 m using triaxial compression tests. The elastic parameters and the obtained triaxial strength for the 5 tested samples are summarized in Table 2. We find that the obtained failure envelope can best be described by the modified Griffith's criterion for compression as expressed in Eq. (1) (see Brady and Brown, 2004). For a representative tensile strength of

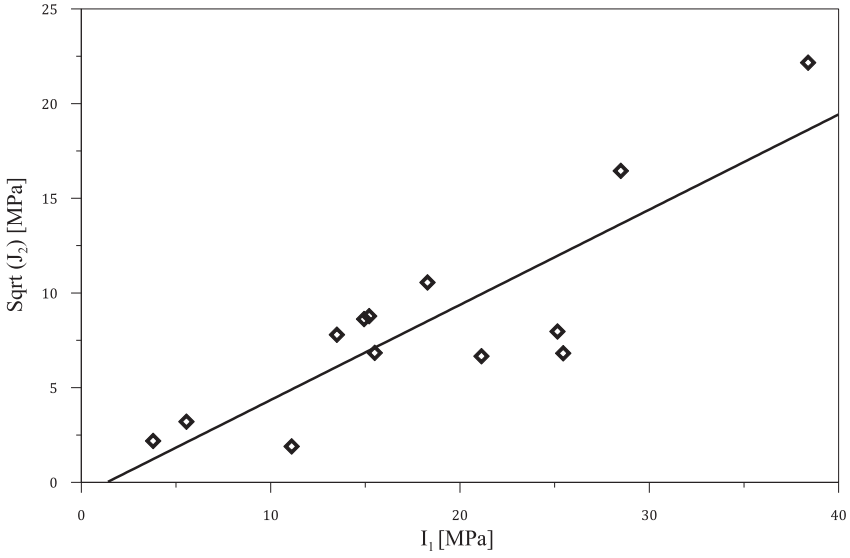

Figure 13. Best-fit linear curve for compression–dilation boundary as found in this study for the Shefela oil shale (*R* squared value of 0.73).

σ_t = 1.75 MPa for samples normal to the bedding direction the actual failure criterion for the tested interval in the Ghareb formation is provided by Eq. (2):

$$\tau^2 = 4\sigma_t(\sigma_n + \sigma_t)\ \text{MPa} \quad (1)$$

$$\tau^2 = 7(\sigma_n + 1.75)\ \text{MPa} \quad (2)$$

where τ and σ_n are shear and normal stresses, respectively. Since the failure criterion strongly depends upon the value of the tensile strength it must be scaled by the value of the tensile strength for each interval in the reservoir. For the tested interval the modified Griffith's criterion for failure in compression is valid up to a maximum principal compressive stress of σ_1 = 19.5 MPa, beyond which it over predicts the actual strength (see Fig. 8). Note that the slight over prediction of strength in the plotted criterion for major principal stress of up to 20 MPa results from the application of a single representative tensile strength value for the entire range.

The static bulk modulus (K) was obtained by linear regression along the linear segment of the hydrostatic pressure vs. total volumetric strain curves (Fig. 9). Two samples were tested in hydrostatic compression, sample AD1-4c from 274 m depth was loaded up to 10 MPa and sample AD1-27b from 341 m depth was loaded up to 30 MPa. Sample AD1-4c exhibited only one linear segment whereas sample AD1-27b exhibited three different linear segments. The slope of each segment is progressively higher, indicating increase in bulk modulus (K_1, K_2, K_3) with increasing hydrostatic pressure. The results are summarized in Table 3. Inspection of Figure 9 reveals that closure of micro-cracks predominates the mechanical response during the first loading segment up to 8 MPa, and indeed the bulk moduli obtained for the two tested samples up to this stress level are similar (see Table 3). The second hydrostatic compression segment between 8 MPa and 20 MPa may be assumed to represent the stage at which the sample exhibits linear elastic deformation. Beyond 20 MPa of hydrostatic compression, the increasing slope (K_3) indicates initiation of irreversible compaction but not yet pore collapse.

4.2. Tensile strength

The distribution of tensile strength results for the Ghareb, Upper, and Lower Mishash formations is shown in Figure 10 as a function of water content for tests performed parallel and normal to the bedding direction. On average, the tensile strength parallel to the bedding is found to be higher by 1.6 ± 0.8 for Ghareb, by 2.29 ± 0.67 for upper Mishash, and by 1.26 ± 0.36 for lower Mishash compared to the tensile strength normal to the bedding. Due to the limited data set and the wide scatter it can only be stated with confidence that the upper Mishash formation exhibits tensile strength anisotropy whereas the results with respect to lower Misash and Ghareb are not statistically conclusive.

The tensile strength seems to slightly decrease with increasing water content in both testing configurations. Similar results were found for Maresha chalks of Lower Eocene by Talesnick et al. (2001).

4.3. Compression–dilation boundary

Although soft rocks like oil shale and chalks are expected to undergo elastic compression (volume reduction) during application of deviator loading, the tested samples from the Shefela basin, both in uniaxial as well as triaxial compression, clearly exhibited dilation (volume growth) beyond some level of stress difference (σ_1–σ_3). The tendency of the rocks to dilate under deviator stress loading may have consequences as to the actual permeability of the rock during oil/gas production when stress concentrations around cavities (e.g. wells) may induce dilation, in contrast to the permeability of rock samples tested at the lab (see next section). There is therefore some merit in seeking the boundary between compressional and dilational response of the rock to deviator loading.

Much of the scientific work on compression–dilation (C–D) boundary in rocks has been done on rock salts which are assumed to be good candidates for hosting hazardous waste disposal because of their low permeability, high thermal conductivity, and creep tendency. The empirical compression–dilation boundary obtained from rock salt bodies from all over the world is typically expressed in terms of the stress invariants as follows:

$$\sqrt{J_2} = aI_1^2 + bI_1 + c \quad (3)$$

where a, b and c are empirical coefficients, I_1 and J_2 are the first and second stress invariants defined as:

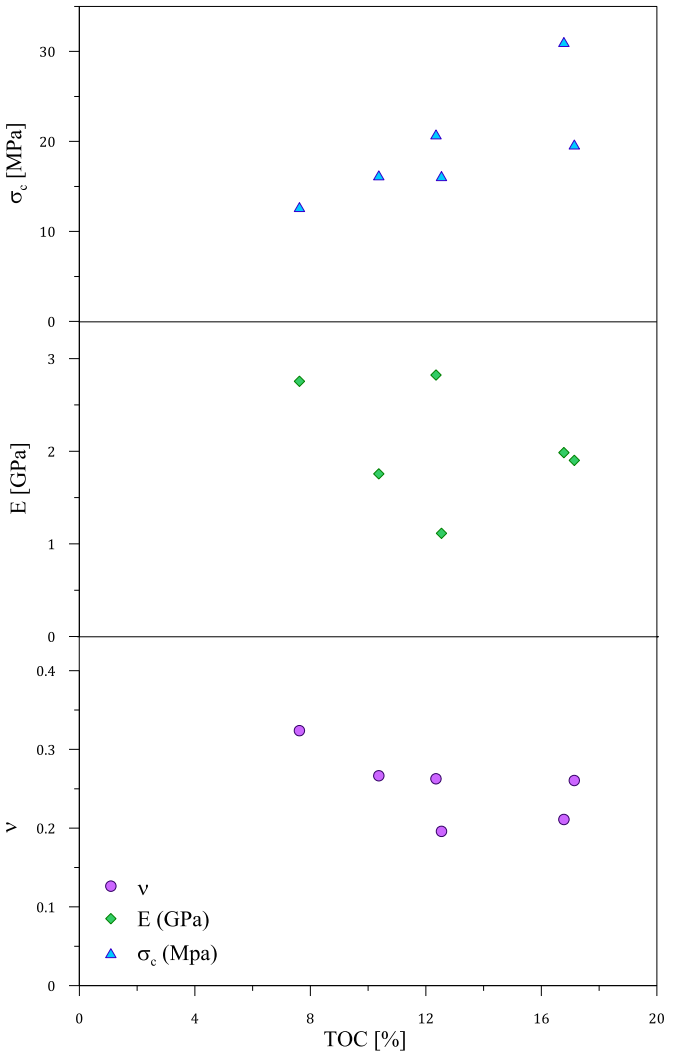

Figure 14. The variation of unconfined compressive strength (top), Young's modulus (center), and Poisson's ratio (bottom) of Ghareb formation with TOC. Figure 11: The variation of tensile strength both parallel (blue circles) and perpendicular (green circles) to bedding direction of Ghareb formation with TOC. (For interpretation of the references to color in this figure legend, the reader is referred to the web version of this article.)

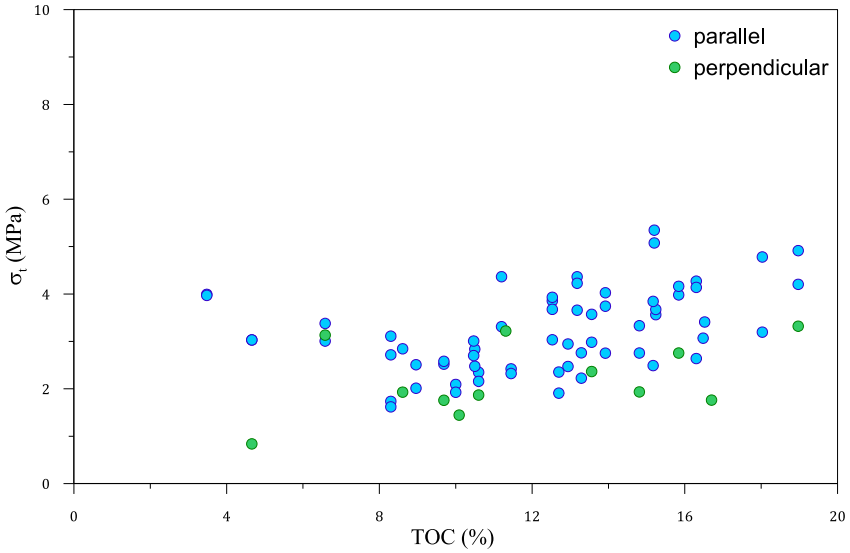

Figure 15. The variation of tensile strength both parallel (blue circles) and perpendicular (green circles) to bedding direction of Ghareb formation with TOC. (For interpretation of the references to color in this figure legend, the reader is referred to the web version of this article.)

$$I_1 = \sigma_1 + \sigma_2 + \sigma_3 \tag{4}$$

$$\sqrt{J_2} = \sqrt{\frac{(\sigma_2 - \sigma_3)^2 + (\sigma_3 - \sigma_1)^2 + (\sigma_1 + \sigma_2)^2}{6}} \tag{5}$$

where σ_1, σ_2, and σ_3 are principal stresses taken at onset of dilation (see Fig. 11). Four empirical compression–dilation boundary criteria are plotted in Figure 12 including data points that were obtained in this study (the fitting coefficients for the models are summarized in Table 4). The C–D boundaries separate the sqrt (J_2) vs. I_1 space into two zones. The lower is the compression zone and the upper is the dilation zone.

It can be noticed that for low mean normal stress ($\sigma_m = (1/3)I_1$) levels ($0 < I_1 < 50$ MPa; $0 < \sigma_m < 17$ MPa) the predictions are nearly similar for all criteria as argued by Van Sambeek et al. (1993). However for higher mean stress levels ($I_1 > 60$ MPa) the deviation between the polynomial expression of Cristescu and Hunsche (1992) and the linear expressions of Spiers et al. (1988) and Ratigan et al. (1991) is large. Hatzor and Heyman (1997) considered mechanical anisotropy in their work on Mount Sedom rock salt and suggested to use two approximately linear boundaries for low mean stress, an upper for compression normal to bedding ($\beta = 0°$) and a lower for compression parallel to bedding ($\beta = 90°$). For a large range of mean stress ($0 < I_1 < 100$ MPa) they suggested to use two second-order polynomial laws for normal and parallel compression.

The data collected for this paper are for relatively low mean normal stress levels (σ_m here is up to ~13 MPa and I_1 is up to ~40 MPa), and for normal compression only. Our results clearly follow a linear compression–dilation boundary trend, as generally suggested by Ratigan et al. (1991) and Spiers et al. (1988) and as found specifically for normal compression by Hatzor and Heyman (1997) for low mean normal stress levels. Naturally, since the rock material tested here is chalk, the actual values of the fitting parameters are different. Nevertheless, for relatively low mean normal stress levels of $0 < \sigma_m < 7$ MPa ($0 < I_1 < 22$ MPa), the C–D boundary for the materials tested here follows previously

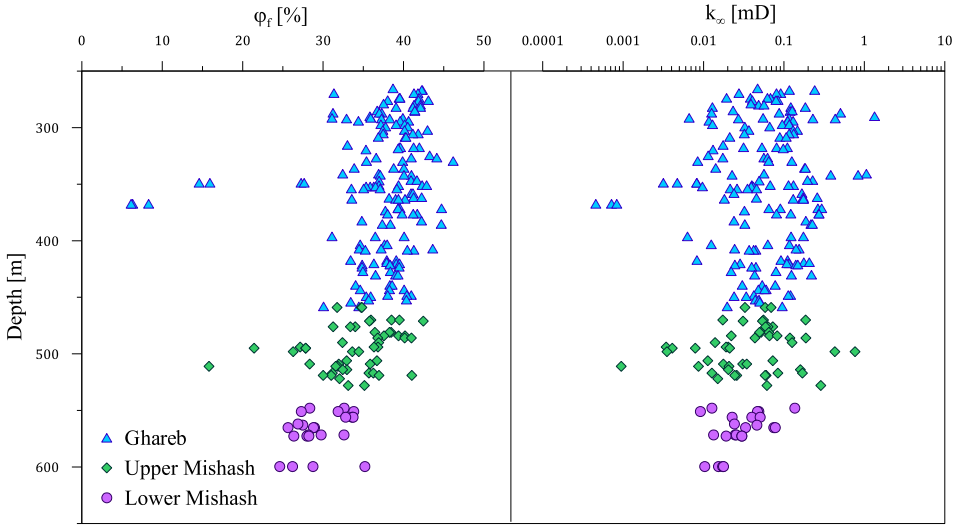

Figure 16. The variation of porosity φ_f (left) and Klinkenberg-corrected gas permeability k_∞ (right) with depth.

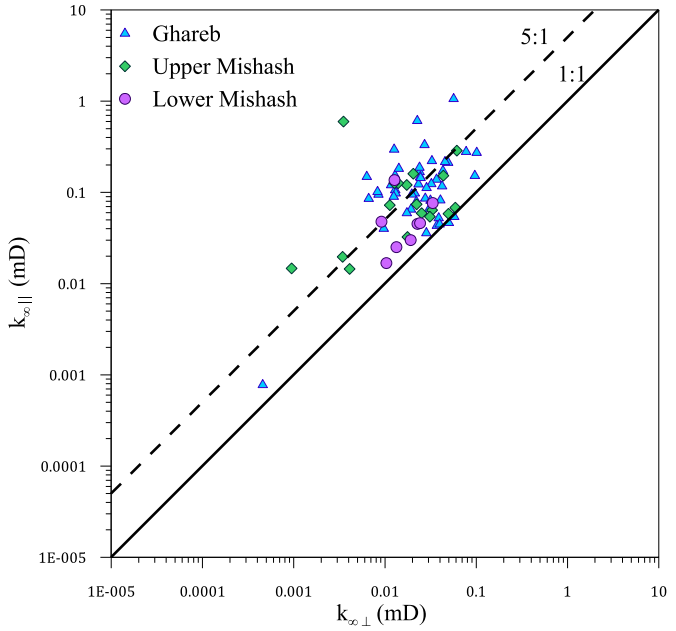

Figure 17. Bedding parallel Klinkenberg-corrected gas permeability $k_{\infty\ \parallel}$ against bedding normal Klinkenberg-corrected gas permeability $k_{\infty\perp}$; black line represents 1:1 reference and purple dashed line represents 5:1 relation. (For interpretation of the references to color in this figure legend, the reader is referred to the web version of this article.)

published criteria. The best-fit linear curve for the results of this study is shown in Figure 13 with the empirical fitting values listed in Table 5.

4.4. Influence of TOC on mechanical behavior

The variation of unconfined compressive strength, Young's modulus, and Poisson's ratio of the Ghareb formation with TOC (%) is shown in Figure 14 and between tensile strength and TOC in Figure 15. Examination of the results plotted in Figure 14 reveals that unconfined compressive strength tends to increase with increasing TOC whereas Young's modulus and Poisson's ratio tend to decrease with increasing TOC although the results are not very conclusive. Tensile strength appears to be independent of TOC (Fig. 15). Closmann and Bradley (1979) have also used the Brazilian test methodology to examine the relationship between tensile strength and organic content in oil shale at room temperature, where the TOC was measured in their work using Fischer Assey. Like us, they have also obtained higher tensile strength when the tensile stress was applied parallel to bedding (they referred to this condition as "fracture normal to bedding" or "fracture across bedding"). But in contrast to our findings their results (their Fig. 6) show marked decrease in tensile strength with increasing Fisher assay whereas our results do not indicate a clear trend (Fig. 15).

It should be pointed out that both unconfined compression and tensile strength tests were performed by us on wet samples with various amounts of initial water contents (Table 1 and Fig. 10, respectively). It is to be expected that the mechanical response would be different when the samples are fully saturated. The influence of TOC on the dynamic elastic moduli of fully saturated oil shale samples is currently being investigated by Shitrit et al. (2015).

The effect of temperature on the mechanical behavior of oil shale was not investigated here. Previous studies suggest that compressive strength, elastic modulus, and tensile strength both parallel and normal to bedding all exhibit marked decrease with increasing temperature (e.g. Closmann and Bradley, 1979).

5. Petrophysical test results

In immature source rocks, or oil shale, the phases that constitute a dry sample are the mineralogical matrix, the kerogen, total organic matter (TOM), and the fluid containing pores. The mass fraction of the oil shale that is kerogen is referred to as total organic matter (TOM). We define the relative volume of fluid containing pores with respect to the total volume of the sample as fluid

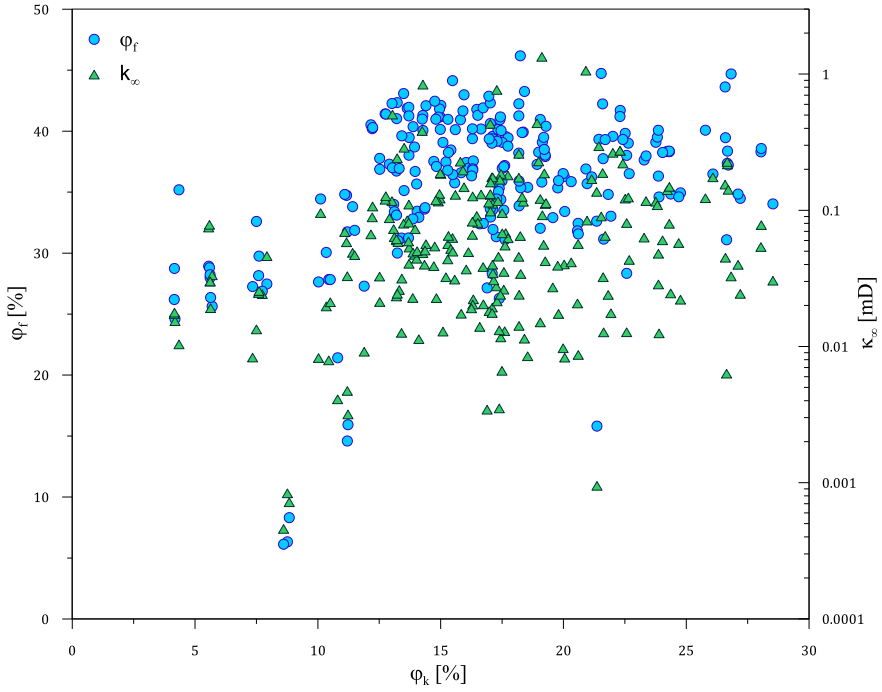

Figure 18. The variation of porosity φ_f and Klinkenberg-corrected gas permeability k_∞ with kerogen content (kerogen volume φ_k).

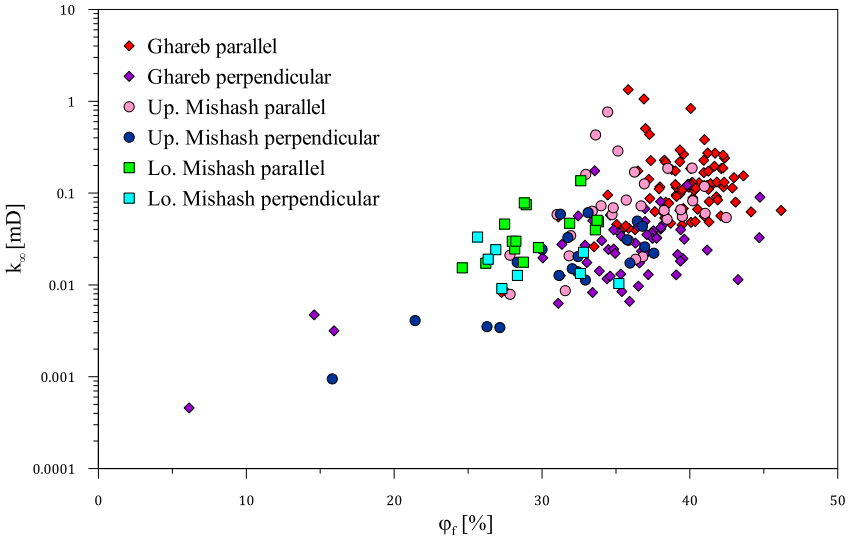

Figure 19. The Klinkenberg-corrected gas permeability k_∞ as a function of fluid porosity ϕ_f.

porosity ($\phi_f = V_p/V$) and the relative volume of kerogen with respect to the total volume of the sample as kerogen volume ($\phi_k = V_k/V$).

The kerogen consists of several elements including carbon, hydrogen, nitrogen, oxygen and sulfur. To calculate the kerogen volume we use the mass fraction of elemental carbon measured directly from the kerogen and the known carbon content from TOC measurements. The carbon content (TOC) divided by the elemental carbon fraction yields the kerogen content (TOM). For the immature oil shale in the Shfela basin, the elemental carbon fraction in the kerogen is ~65%. Therefore, the kerogen mass fraction is TOM (wt%) = 1.54 × TOC (wt%). The kerogen volume ϕ_k is obtained by multiplying the TOM by the bulk density and dividing by the kerogen density which was found to be on average 1.4 g/cm^3.

Like other chalks, the fluid porosity ϕ_f of the Shefela oil shale is relatively high, averaging 37%, and constant throughout the Ghareb formation. The fluid porosity decreases with depth averaging 32% at the Mishash formation (Fig. 16). The decrease in ϕ_f is likely due to the observed increase in silicification of the chalk in the Mishash formation relative to the Ghareb and less likely due to compaction given the Ghareb's relatively constant porosity.

The Klinkenberg-corrected gas permeability (Klinkenberg, 1941) k_∞ is relatively tight, ranging between 0.001 mD and 1 mD depending on depth and flow direction. In the Ghareb formation the average value of $k_{\infty,h}$ is 0.15 mD for flow parallel to the bedding direction and $k_{\infty,v}$ is 0.03 mD for normal to the bedding direction. In the Mishash, $k_{\infty,h}$ decreases to an average value of 0.09 mD and an average value of 0.02 mD for $k_{\infty,v}$ (Fig. 12). Our results show a permeability anisoptropy of k_v/k_h~0.2 on average through the entire investigated interval of the Aderet well, implying that vertical flow in the field is five times more restricted relative to horizontal flow along the generally horizontally dipping bedding planes (Fig. 17).

The fluid porosity is found to be independent of variations in the kerogen volume (see Fig. 18), confirming co-precipitation of the kerogen and calcite minerals during deposition. This is consistent with the observation that the chalk consists primarily of nanoplankton. The Klinkenberg-corrected gas permeability is also independent of the kerogen volume (see Fig. 18). This suggests the permeability is controlled by the inter-granular pores and not the kerogen even though the kerogen volume is comparable to the fluid porosity, (see Fig. 19).

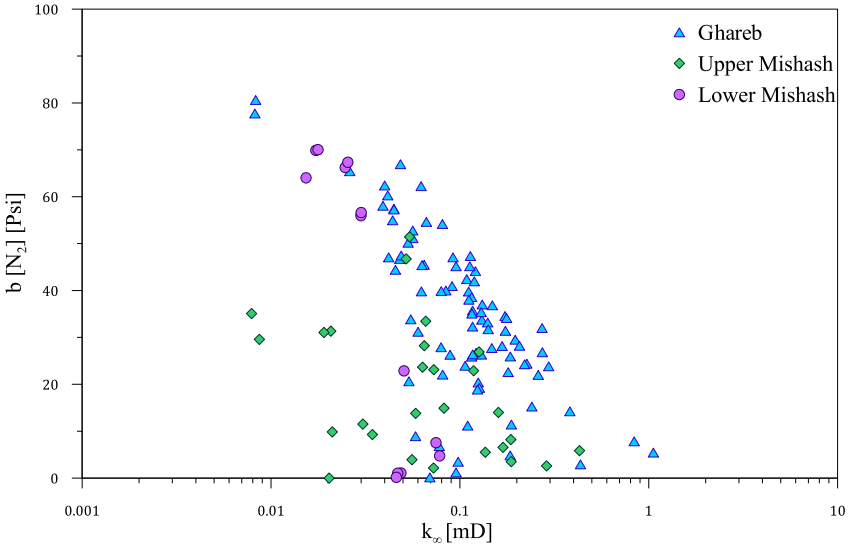

Figure 20. The relationship between slip factor b and Klinkenberg-corrected gas permeability k_∞ for Ghareb and upper Mishash and lower Mishash Formations.

Figure 20 shows the measured slip factor b as a function Klinkenberg corrected-permeability. Measured values show the typical inverse relationship between b and k_∞ with values reaching as high as 80 psi at 0.009 mD. Given that b is inversely proportional to the pore throat radius, the high measured values of b imply extremely small pore throats in the chalk on the scale of tens of nanometers. This underscores the importance of including the Klinkenberg correction when considering gas-phase production from these organic chalk systems.

6. Conclusions

The mechanical and petrophysical properties of the Shefela organic-rich chalk are explored in this paper. The following conclusions can be made from this study:

- At room temperature, the chalk exhibits a brittle behavior, the compressive strength failure criterion of which can be best described by the non-linear Griffith's criterion.
- The chalk is characterized by high porosity up to 45% and very low permeability of ~0.09 mD.
- The deeper, more silicified Mishash formation shows decreasing porosity and permeability with increasing mechanical strength relative to the Ghareb formation.
- The chalk displays both mechanical and petrophysical anisotropy. The vertical to horizontal permeability and tensile strength ratios were found to be $k_v/k_h = 0.25$ and $\sigma_{t,v}/\sigma_{t,h} = 0.5$.
- Tensile strength and elastic moduli of initially wet, but not fully saturated, carbon rich chalks appear to be independent of organic content, whereas the compressive strength of such samples appears to increase with increasing organic content.
- The porosity and permeability are independent of variations in organic content, confirming co-precipitation of the calcite minerals and organic matter during deposition.

Acknowledgment

This research was funded by Israel Energy Initiative Ltd through BGU contract No.87244811. The financial support of IEI is greatly appreciated.

References

Almogi-Labin, A., Bein, A., Sass, E., 1993. Late cretaceous upwelling system along the southern tethys margin (Israel) - interrelationship between productivity, bottom water environments, and organic-matter preservation. Paleoceanography 8, 671–690.
Brady, B.H.G., Brown, E., 2004. Rock Mechanics for Underground Mining, third ed. Kluwer Academic Publishers, London.
Burg, A., Bartov, Y., Grosman, R., Dror, Y., 2010. Survey of the Shfela't Yehuda Oil Shale. Examination Drillings at Nahal Guvrin and Aderet, Drilling Process and Geological and Hydrological Preliminary Conclusions. IEI, Jerusalem.
Closmann, P.J., Bradley, W.B., 1979. EFFECT of temperature on tensile and compressive strengths and Youngs modulus of oil-shale. Soc. Petrol. Eng. J. 19, 301–312.
Critescu, N.D., Hunsche, U.E., 1992. Determination of a Nonassociated Constitutive Equation for Rock Salt From Experiments.
Dyni, J.R., 2003. Geology and resources of some world oil-shale deposits. Oil Shale 20, 193–252.
Eshet, Y., Almogi-Labin, A., Bein, A., 1994. Dinoflagellate Cysts, Paleoproductivity and upwelling systems - a Late Cretaceous example from Israel. Mar. Micropaleontol. 23, 231–240.
Gvirtzman, G., Moshkovitz, S., Reiss, Z., 1985. Senonian to early eocene mount scopus group in the hashefela region, Central Israel - stratigraphy and Basin Evolution. Israel J. Earth Sci. 34, 172–192.
Hatzor, Y.H., Heyman, E.P., 1997. Dilation of Anisotropic Rock Salt: Evidence From Mount Sedom Diapir.
Hutton, A.C., 1987. Petrographic classification of oil shales. Int. J. Coal Geol. 8, 203–231.
IEA, 2010. World Energy Outlook 2010. OECD, Paris, p. 165.
Klinkenberg, L.J., 1941. The Permeability of Porous Media to Liquids and Gases. Drilling and Production Practice. American Petroleum Inst, pp. 200–213.
Meilijson, A., Ashckenazi-Polivoda, S., Ron-Yankovich, L., Speijer, R.P., Illner, P., Alsenz, H., Almogi-Labin, A., Feinstein, S., Berner, Z., Püttmann, W., Abramovich, S., 2014. Chronostratigraphy of the Upper Cretaceous high productivity sequence of the Southern Tethys, Israel. Cretac. Res. 50, 187–213.
Minster, T., 2009. Oil shale deposits in Israel. Geological Survey of Israel.
Ratner, M., Tiemann, M., 2014. An Overview of Unconventional Oil and Natural Gas: Resources and Federal Actions. CRS Report R43148.
Ratigan, J.L., Van Sambeek, L.L., DeVries, K.L., Nieland, J.D., 1991. The Influence of Seal Design on the Development of Disturbed Rock Zone in the WIPP Alcove Seal Tests.
Ryan, R.C., Fowler, T.D., Beer, G.L., Nair, V., 2010. Shell's in situ conversion process—from laboratory to field Pilots. In: Ogunsola, O.I., Hartstein, A.M., Ogunsola, O. (Eds.), Oil Shale: a Solution to the Liquid Fuel Dilemma, ACS Symposium Series. American Chemical Society, Washington, DC, pp. 161–183.
Spiers, C.J., Peach, C.J., Brzesowsky, R.H., Schutjensm, P.M.T.M., Liezenberg, J.L., Zwart, H.J., 1988. Long Term Rheological and Transport Properties of Dry and Wet Salt Rocks.
Shitrit, O., Hatzor, Y.H., Feinstein, S., Rosenberg, Y.O., Vinegar, H.J., 2015. Constitutive model of mechanical properties of bituminous chalk with high porosity and TOC content, central Israel. In: Hassani, F. (Ed.), 13 ISRM Congress, Montreal Canada.
Spiro, B., 1980. Geochemistry and Mineralogy of Bituminous Rocks in Israel. Hebrew University, Jerusalem.
Talesnick, M.L., Hatzor, Y.H., Tsesarsky, M., 2001. The elastic deformability and strength of a high porosity, anisotropic chalk. Int. J. Rock Mech. Min. Sci. 38, 543–555.
Tissot, B.P., Vandenbroucke, M., 1983. Geochemistry and pyrolysis of oil shales. Abstr. Pap. Am. Chem. Soc. 185, 53 (Geoc).
Tissot, B.P., Welte, D.H., 1984. Petroleum Formation and Occurrence. Springer, Berlin.
Van Sambeek, L.L., Ratigan, J.L., Hansen, F.D., 1993. Dilatancy of rock salt in laboratory tests. Int. J. Rock Mech. Min. Sci. Geomech. Abstr. 30 (7), 735–738.